Sixth International Symposium on Physics of Fluids (ISPF6)
International Journal of Modern Physics: Conference Series
Vol. 42 (2016) 1660186 (15 pages)

LARGE-EDDY SIMULATION OF SHOCK-WAVE/TURBULENT BOUNDARY LAYER INTERACTION AND ITS CONTROL USING SPARKJET

YANG GUANG[1], YAO YUFENG[2], FANG JIAN[1], GAN TIAN[1], and LU LIPENG[1]

[1]*National Key Laboratory of Science and Technology on Aero-Engine Aero-Thermodynamics, School of Energy and Power Engineering, Beihang University, Beijing 100191, China*

[2]*Faculty of Environment and Technology, University of the West of England, Bristol BS16 1QY, United Kingdom*

Published 22 June 2016

Large-eddy simulation (LES) of an oblique shock-wave generated by an 8° sharp wedge impinging onto a spatially-developing Mach 2.3 turbulent boundary layer and their interactions has been carried out in this study. The Reynolds number based on the incoming flow property and the boundary layer displacement thickness at the impinging point without shock-wave is 20,000. The detailed numerical approaches are described and the inflow turbulence is generated using the digital filter method to avoid artificial temporal or streamwise periodicity. Numerical results are compared with the available wind tunnel PIV measurements of the same flow conditions. Further LES study on the control of flow separation due to the strong shock-viscous interaction is also conducted by using an active control actuator "SparkJet" concept. The single-pulsed characteristics of the control device are obtained and compared with the experiments. Instantaneous flowfield shows that the "SparkJet" promotes the flow mixing in the boundary layer and enhances its ability to resist the flow separation. The time and spanwise averaged skin friction coefficient distribution demonstrates that the separation bubble length is reduced by maximum 35% with the control exerted.

Keywords: Large-Eddy simulation; shock-wave/turbulent boundary layer interaction; SparkJet control.

1. Introduction

Shock-wave/turbulent boundary layer interaction (SWTBLI) happens ubiquitously in high-speed vehicles, including transonic airfoils, supersonic inlets, control surfaces of aircrafts, missile base flows, reaction control jets, and over-expanded nozzles. Among these configurations, maximum mean and fluctuating wall pressure and thermal loads are often found in the vicinity of SWTBLI region and they can cause serious aerodynamic and structural problems.[1] Over the past sixty years, the SWTBLI phenomenon has been investigated over a wide range of configurations and flow conditions. Although

substantial databases of experimental[2] and theoretical[3] results have been accumulated, the underlying physical flow phenomenon is still not fully understood and remains one major subject of active investigation due to its great practical importance and extreme complexity. Some extensive reviews on the achievements and remaining challenges were given previously by Green[4], Adamson and Messiter[5], Delery[6], Dolling[1] and most recently by Knight[7] as well as Babinsky and Harvey[8].

With the rapid increase of computing power in recent decades, especially the fast development of high-performance computing (HPC) platforms, modern computational fluid dynamics (CFD) technique is now playing a much more important role in aerodynamic researches. In particular, Direct Numerical Simulation (DNS) and Large-Eddy Simulation (LES) become effective tools for turbulence mechanism researches[9, 10]. LES can capture important flow dynamics with a significantly reduced computing force than that of DNS, thus makes it an ideal tool when DNS is too expensive, such like relatively high Reynolds number flow.

An important problem of SWTBLI flow is that the strong adverse pressure gradient due to shock-wave impinging can trigger large-scale flow separation, resulting in significant total pressure loss and flow distortion. Hence, controlling the shock-wave induced flow separation is always a focus in SWTBLI researches and many active and passive control approaches have been proposed[11]. Passive control devices include vortex generators[12-14], Mesoflaps[15-17], ventilation duct or porous wall over cavity[18, 19], etc. Active controls using plasma is now gaining more and more attentions in high-speed flows for their advantages of avoiding any *ad hoc* mechanical components, enabling high effectiveness and ability of high-frequency modulation.

Active control of SWTBLI flow separation by a "SparkJet" actuator was numerically studied in this paper. The actuator device was invented by Cybyk *et al.*[20] and the primary aim was for high-speed flow control application. This actuator can manipulate high-speed flow without introducing additional mechanical components. Fig. 1 shows a single cycle of SparkJet operation which consists of three distinct stages: energy deposition, discharge, and refilling. Fig. 2 is the photographical view of a Laboratory SparkJet device which is a modified version of Cybyk's original invention, experimentally investigated by Reedy *et al.*[21]. Characteristics of this device have been extensively investigated in experimental studies[22-31].

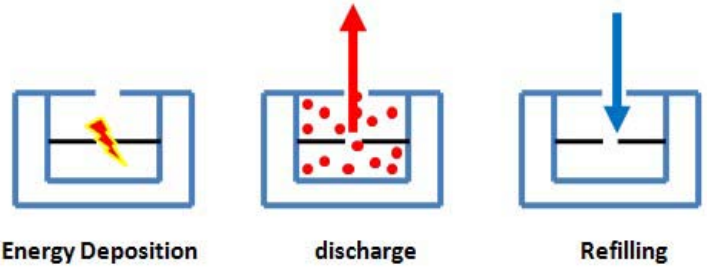

Fig. 1. Schematic of SparkJet work cycle.

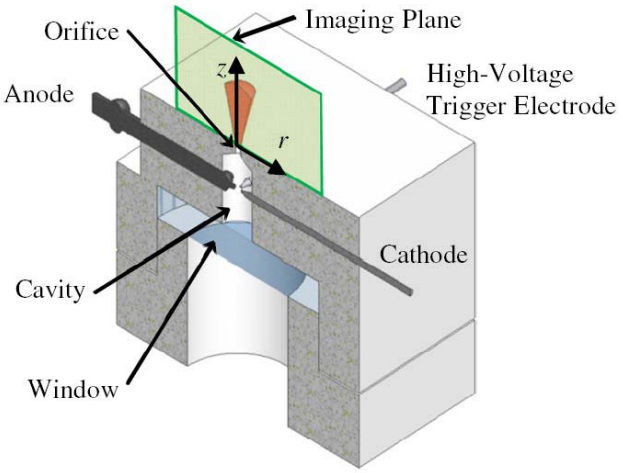

Fig. 2. SparkJet device used in the experiment of Reedy *et al*.[21]

The purpose of this paper is to validate numerical predictions obtained by Large-Eddy Simulation of SWTBLI flow and further explore the feasibility of SWTBLI separation control using the SparkJet device.

2. Numerical Approach

The numerical approach adopted in this paper is Large-Eddy Simulation due to its advantages mentioned in the introduction. The conceptual idea of LES is to fully resolve the large-scale energy-containing turbulence structures and only model the effect of the unresolved smaller scales of turbulent flow. The spatial-scale separation is represented by the convolution product defined in Eq. (1):

$$\bar{q} = \int G(\boldsymbol{x} - \boldsymbol{z}; \overline{\Delta})\, q(\boldsymbol{z}) d^3\boldsymbol{z} \ , \tag{1}$$

where q is an arbitrary variable, $\bar{q}$ is the filtered variable, G the filter convolution kernel, and Δ its associated characteristic cutoff length scale. The kernel function G satisfies that:

$$\int G(\boldsymbol{x} - \boldsymbol{z}; \overline{\Delta})\, d^3\boldsymbol{z} = 1 \ . \tag{2}$$

In compressible flow researches, the following Favré average is a common used technique to take account of the effect of density variety,

$$\tilde{q} = \frac{\overline{\rho q}}{\bar{\rho}} \ . \tag{3}$$

Applying the above grid filter and Favré average operator to the Navier-Stokes (N-S) equations and after some algebraic manipulations, an estimated form of the grid-filtered dimensionless compressible N-S equations can be written as:

$$\frac{\partial \bar{\rho}}{\partial t} + \frac{\partial \bar{\rho}\tilde{u}_i}{\partial x_i} = 0 \ , \tag{4}$$

$$\frac{\partial \bar{\rho}\tilde{u}_i}{\partial t} + \frac{\partial \bar{\rho}\tilde{u}_i\tilde{u}_j}{\partial x_j} + \frac{\partial \bar{p}}{\partial x_i} - \frac{1}{Re}\frac{\partial \bar{\tau}_{ij}}{\partial x_j} \approx -\frac{\partial \sigma_{ij}}{\partial x_j} \frac{\partial \bar{\rho}}{\partial t} + \frac{\partial \bar{\rho}\tilde{u}_i}{\partial x_i} = 0 \ , \tag{5}$$

$$\frac{\partial \bar{E}_t}{\partial t} + \frac{\partial (\bar{E}_t + \bar{p})\tilde{u}_j}{\partial x_j} - \frac{1}{Re}\frac{\partial \bar{\tau}_{ij}\tilde{u}_i}{\partial x_j} + \frac{1}{(\gamma-1)RePrM^2}\frac{\partial}{\partial x_j}\left[\tilde{\mu}\frac{\partial \tilde{T}}{\partial t}\right] \approx -\tilde{u}_i\frac{\partial \sigma_{ij}}{\partial x_j} - \frac{1}{(\gamma-1)M^2}\frac{\partial}{\partial x_j}\left[\bar{\rho}\Theta_j\right], \tag{6}$$

where σ_{ij} is the subgrid-scale (SGS) stress tensor and Θ_j is the SGS heat flux and defined as:

$$\sigma_{ij} = \bar{\rho}\left(\widetilde{u_i u_j} - \tilde{u}_i\tilde{u}_j\right) \ , \tag{7}$$

$$\Theta_j = \left(\widetilde{Tu_j} - \tilde{T}\tilde{u}_j\right) \ . \tag{8}$$

The SGS stress are determined by SGS model, and the SGS model used in present simulation is the Mixed-Time-Scale model by Inagaki *et al.*[32]. The detailed derivation of the above equation and the validity of the estimation can be found in Vreman *et al.*[33]

The above equations are solved by using an in-house high order finite-difference code SBLI. The code employs a fourth-order central difference scheme to calculate derivatives at internal points. Close to boundaries, a stable boundary treatment by Carpenter *et al.*[34] is applied, giving the overall fourth-order accuracy. Time integration is based on a third-order compact storage Runge-Kutta method[35]. An entropy splitting approach of Sandham *et al.*[36] is used to calculate the nonlinear terms, which will guarantee the stability of the algorithm. A TVD shock capturing scheme and the artificial compression method (ACM) of Yee *et al.*[37], coupled with the Ducros sensor[38], are implemented in the code to handle shock-waves and contact discontinuities. The code is made parallel using the MPI library. A multi-block version of the code was extensively validated by Yao *et al.*[39].

As for the boundary condition, periodic boundary conditions are used in the spanwise direction. At the wall, the no-slip condition is enforced. Furthermore, the wall is considered isothermal with a temperature close to the upstream adiabatic value (assuming a recovery factor of 1). The top (free-stream) and outflow boundaries make use of the characteristic non-reflecting boundary condition[40] in order to minimize unwanted reflections from the computational-box boundaries. The oblique shock-wave is introduced at the top boundary using the Rankine–Hugoniot relationships. The turbulent inflow turbulence is generated using a digital filter method[41] in present simulation.

3. SWTBLI Results

As mentioned before, the simulation flow condition is consistent with the experiment performed by Dupont *et al.* [42] at IUSTI, i.e. an oblique shock-wave generated by an 8° sharp wedge impinging onto a Mach 2.3 turbulent boundary layer. The flow parameters are listed in Table 1. The Reynolds number is based on the boundary layer displacement

thickness at interaction point without shock-wave impingement. This flow condition has been previously studied by Garnier *et al.*[43] and Touber and Sandham[44], also using LES.

Table 1 Flow parameters.

Mach number	Wedge angle (°)	Stagnation Pressure (bar)	Stagnation Temperature (K)	Reynolds number	Sutherland's law C value
2.3	8.0	0.5	300.0	20000.0	0.76

In present simulation, the computation domain is (L_x, L_y, L_z) = (256mm, 51mm, 59mm), along the streamwise, the wall-normal and the spanwise directions, respectively. For the convenience of comparing with the experimental data, the streamwise domain range is [148mm, 404mm], which is the same as the physical domain seen in the experiment. The shock-wave impinging point is at x = 336mm in absence of shock-wave. The grid numbers in each direction are (N_x, N_y, N_z) = (451, 151, 281), uniformly distributed in the streamwise and the spanwise directions while highly stretched in the wall normal direction. The corresponding grid resolution in each direction is estimated as $(\Delta x^+, \Delta y^+, \Delta z^+)$ = (33, 1.3, 12), which satisfies the general LES requirement[45].

Fig. 3 shows the mean streamwise velocity profile at x = 260mm where the flow is supposed to be fully developed equilibrium turbulent boundary layer before the interaction. It can be seen that the LES computation results are in good agreement with that from the PIV measurement, and the van-Driest transformed velocity profile also agrees well with the classic log-law of the wall. This indicates that the flow is indeed fully developed turbulent boundary layer in the region ahead of shock-wave impinging location.

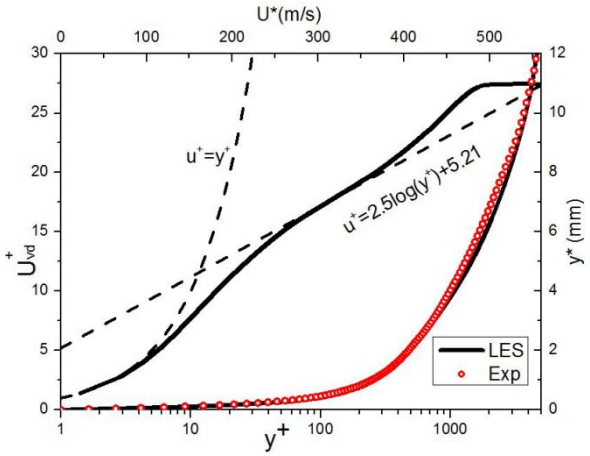

Fig. 3. Velocity profile at x = 260mm (the superscript * means in dimensional form).

Fig. 4(a) shows the skin friction coefficient, while Fig. 4(b) is the wall pressure distribution (normalized by incoming free-stream static pressure). The results are compared with the LES results of Touber and Sandham[44], and reasonable agreements are

achieved. The wavy profile of the skin friction may be due to the lack of statistical samples. We can see from the figure that the flow separates at x = 295.32mm and reattaches at x = 334.67mm, resulting a mean separation bubble length of about 39.4mm.

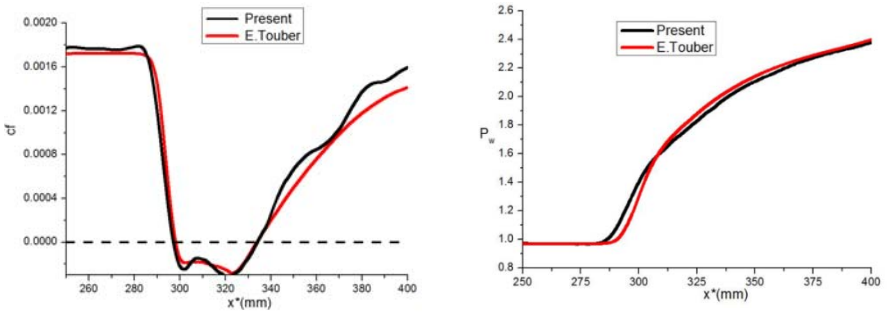

(a) (b)

Fig. 4. (a) Skin friction coefficient, (b) wall pressure profiles.

Fig. 5 shows the comparison of the mean streamwise of LES predications and PIV measurements at five successive streamwise locations. It can be seen some noticeable influences of adverse pressure gradient on the development of the boundary layer's shape across the entire interaction zone. Overall, the LES results are in good agreements with the PIV data. The boundary layer thickening process is well captured according to the mean streamwise profile evolution. Generally, the LES predictions and PIV measurements agree extremely well in both upstream and downstream of the interaction, while some discrepancies are observed in the interaction zone where the flow is unsteady and complex, thus difficult to simulate or measure accurately. Fig. 6 gives the Reynolds stress distributions. Although the Reynolds stress is hard to be accurately obtained using PIV, the qualitative or even the quantitative agreement between the PIV and the LES is remarkably good.

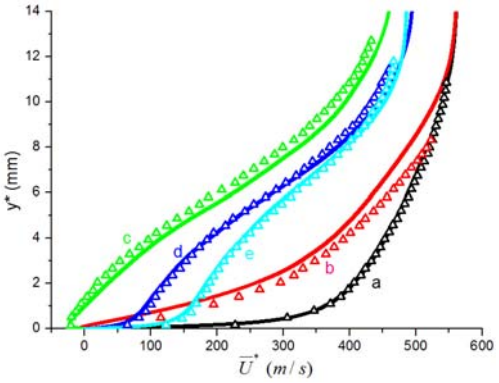

Fig. 5. Mean streamwise velocity. profiles at different streamwise locations *where* a, b, c, d, e correspond to $x^\star$ = 275mm, 300mm, 325mm, 350mm, 375mm, respectively.

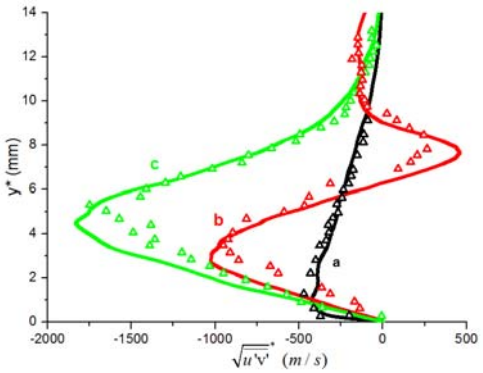

Fig. 6. Reynolds shear-stress field: profiles at different streamwise locations where *a, b, c* correspond to x^* = 280mm, 321mm, 345mm, respectively.

As for the instantaneous flow structure, Fig. 7 shows the instantaneous numerical Schlieren (by using density gradient magnitude) and the streamwise velocity fluctuation at the plane of $y^+ = 15$. The shock-wave system is clearly captured and the typical low-speed streaks of the equilibrium turbulent boundary layer can be clearly observed before entering the interaction region. In the interaction region, the streaks are broken and gradually recovered after the reattachment. Fig. 8 shows the instantaneous shock-wave surface and the vertical structure identified by Q criterion in the boundary layer, both the shockwave and the turbulent coherent structures are well captured in our numerical simulation.

In general, the LES results, including both the mean profile and the second-order turbulence statistics, agree sufficiently well with the PIV measurements, thus the ability of present LES to reproduce the complex flow field of SWTBLI is verified.

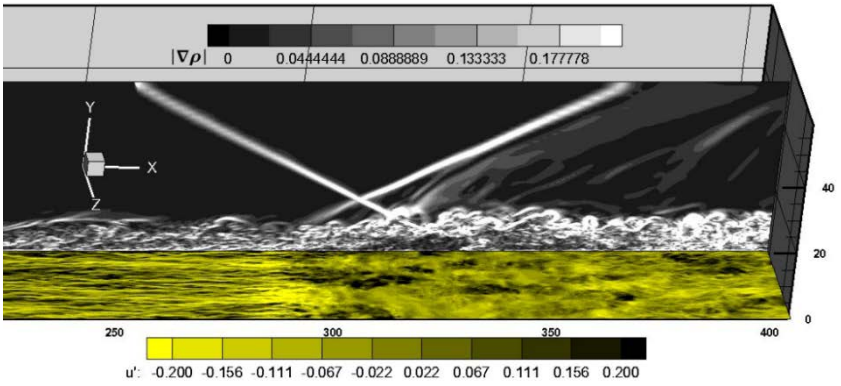

Fig. 7. Instantaneous flow structure, numerical Schlieren of shock-wave and boundary layer streaks.

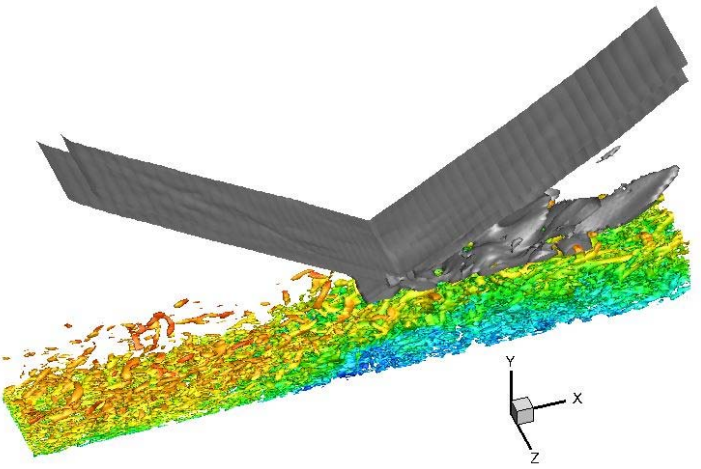

Fig. 8. Instantaneous flow structures. The vertical structures are identified by Q criterion and colored by streamwise velocity. The shock wave surface is identified by the magnitude of pressure gradient.

4. SparkJet Control

In this section, further LES is carried out to study the detailed flow field resulting from the SparkJet control applied to the same SWTBLI flow configuration as shown above. The SparkJet device is placed before the separation zone. The geometrical configuration parameters are chosen in reference to the real device in experiment[21]. For the purpose of the proof of concept, rectangular subdomain was adopted in present computations, rather than the cylinder shape used in experiments. The energy deposition process of electrical discharge heating performed during the test is modeled by introducing an additional heating source in the total energy equation.

We adopted a relative narrower spanwise computational domain here to avoid redundant calculations and massive storage space of long time integration, and the non-control base flow with the same spanwise is also carried out for comparisons. The spanwise length here is larger than the narrowest case presented in the LES of Touber and Sandham[46], in which the validity of results has been verified in details. The computation domain of the base flow is (L_x, L_y, L_z) = (256mm, 51mm, 14.0mm), the streamwise domain range is also [148mm, 404mm], same as those described in the above section. The center of the device is placed at x = 280mm, 1.5 boundary layer nominal thickness before the separation line. The throat size is (L_x, L_y, L_z) = (2mm, 1mm, 2mm), while the cavity is a cubic of (L_x, L_y, L_z) = (6mm, 6mm, 6mm). Fig. 9 shows the geometry of the SparkJet actuator model in present simulation. This control device geometry is comparable with that used in UIUC's experiment[21]. In the UIUC experiment, the cavity volume is 183mm^3 and jet is exhausted through a 0.83-mm-diameter orifice, while in present simulation the cavity volume is 216mm^3 and the jet flow is exhausted through a squared throat of 4mm^2. The numbers of computational grids in each block are given in the following Table 4.

Table 2 Total Grid numbers of three computational domains.

	Nx	*Ny*	*Nz*
Main flow	600	150	150
Throat	30	10	30
Cavity	90	60	90

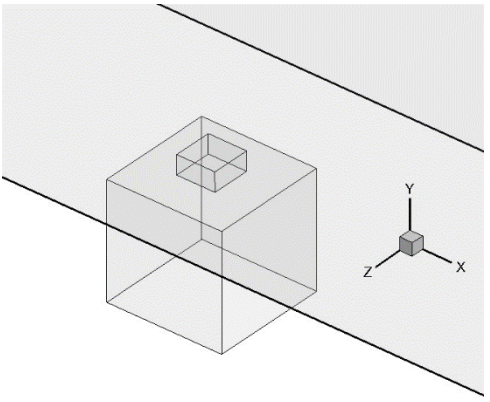

Fig. 9. SparkJet control device geometry in present simulation.

The heating source pulse is distributed spherically from the center of the cavity domain and explicitly given by the following formula, which was proposed by Zheltovdov et al.[47, 48] as the Energy Deposition (ED) model in their simulation:

$$q = q_0 H(t) exp\left[-\left(\frac{x-x_0}{R_x}\right)^2 - \left(\frac{y-y_0}{R_y}\right)^2 - \left(\frac{z-z_0}{R_z}\right)^2\right], \quad (9)$$

$$H(\mathrm{t}) = \begin{cases} 1 & 0 \le \mathrm{mod}(\mathrm{t}, 1/f) < \tau \\ 0 & \tau \le \mathrm{mod}(\mathrm{t}, 1/f) \le 1/\mathrm{f} \end{cases}. \quad (10)$$

In the formulae above, the parameter q_0 decides the spark heating intensity, (x_0, y_0, z_0) is the center of the heating source, (R_x, R_y, R_z) represents the energy concentration radius, f is the pulse frequency, and τ is the heating duration in each pulse. In present simulation, the heating source is positioned at the center of the cavity cubic, the radius (R_x, R_y, R_z) are set as 2mm, non-dimensional heating intensity q_0 is 0.15. Integrating the heating source over time and space we get the total added energy Q. The total deposited energy Q here is 8.9J in a time duration of $\tau = 20\mu s$. The choosing of the energy source parameters is also in reference to the UIUC experiment. In the experiment, they tested three different energy levels, e.g. 41 mJ, 330 mJ, and 4.0 J, the heating duration is also 20μs. The simulation condition is comparable to the highest energy level case of the experiment. As we focused on the characteristics of a single-pulse, the pulse frequency f is not involved here, the flow field is sampled every 4μs in a time span of 1000μs after energy deposition starts.

Fig. 10 gives the instantaneous numerical Schlieren of the controlled flow field at the spanwise middle plane and an enlarged view near the control device. The streamline in the cavity and near the throat is also shown, from which the interaction between the ejected jet flow and the main crossflow can be observed. Also we can see that in the cavity, the air explodes from the center to the surrounding walls after the energy deposition process started. At the upper exit plane of the cavity domain, a jet stream is formed and ejected into the main crossflow. It can be seen that because of the high momentum of supersonic boundary layer, the jet was suppressed in the near-wall region of the boundary layer. The height of the jet was located between 10-20% of the local boundary layer thickness. However, it still has an obvious influence on the downstream interaction zone.

Fig. 11 plots the maximum speed of the jet at the exit of the control cavity. It can be seen that in a short time period after the energy deposition, the air in the cavity will be exploded and ejected into the main crossflow, at rapidly increased velocity up to the maximum peak value. And then the discharge velocity will be gradually declined to the minimum value close to zero, followed by a slow recovery phase. The highest jet velocity predicted from LES is about 446m/s. The measurements of UIUC's experiment on SparkJet in a quiescent environment are also shown in Fig. 11 As the control parameters in present simulation are close to the highest energy level (4.0J) case, a corresponding higher jet speed is also expected, close to that of experimental data. However, the time history of maximum velocity from LES prediction exhibits a rapid decay after the peak, which may be due to a larger jet exit area used in present simulation.

Fig. 12(a) shows the time averaged wall pressure distribution on the middle plane and side plane of the controlled case, the distribution are similar except the singularity position where the control device locates. And compared with the uncontrolled case, the pressure has a deeper arise and the pressure plateau is shorter, which reflects a reduction of separation zone. Fig. 12(b) shows the time- and the spanwise-averaged skin friction coefficient variations along the streamwise direction. Compared with the uncontrolled base flow, it can be seen that the flow separation is delayed resulting an overall separation length reduction. The time- and the spanwise-averaged separation bubble length of the control case study is 31mm, about 35% decrease compared to that of the uncontrolled case.

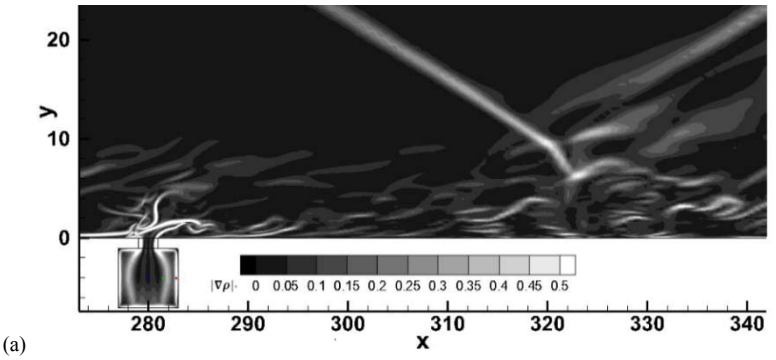

(a)

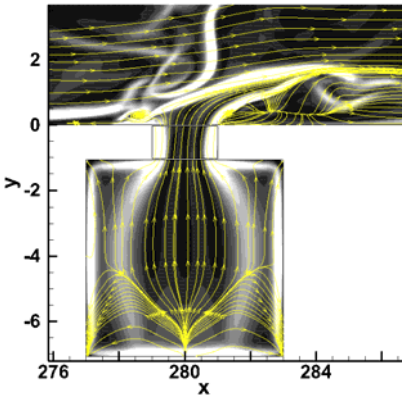

(b)

Fig. 10. Numerical Schlieren of controlled flow field at $t = 40\mu s$. A zoomed flow field near the cavity is shown in (b).

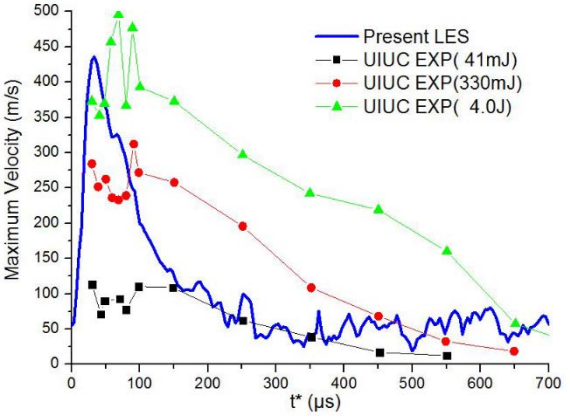

Fig. 11. Maximum jet velocity at the exit of the throat.

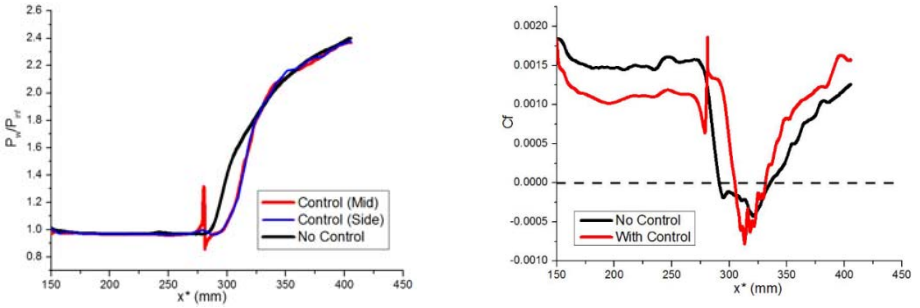

(a) (b)

Fig. 12. (a) Skin friction coefficient, and (b) wall pressure profiles.

5. Conclusions

Large-Eddy Simulation of a Mach 2.3 shock-wave generated by an 8° sharp wedge impinging onto a spatially-developing turbulent boundary layer along a flat plate is carried out. The numerical approaches and the simulation results are validated with experimental measurements and other LES results in the same flow condition. Based on this, a "SparkJet" control technique is further studied using LES. The configuration of the control device is modeled in reference to the previous experiments with similar configuration parameters. The single-pulse characteristics of the control mechanism are analyzed. The maximum jet velocity time history agrees qualitatively well with the experiments and a maximum jet velocity of 446m/s is predicted, close to that of experimental measurement. By exerting the control device, the flow separation is delayed noticeably and the size of the separation bubble is also reduced significantly by about 35%, and this proves the effectiveness of the SparkJet control technique on suppressing the flow separation occurred in SWTBLI flows.

Acknowledgement

This work is supported by the National Natural Science Foundation of China (51420105008, 11302012), the National Basic Research Program of China (2012CB720205), and the Astronautical Technology Innovation Foundation of China. The computational time for the present study was provided by the UK Turbulence Consortium (EPSRC grant EP/L000261/1) and the simulations were run on the UK High Performance Computing Service ARCHER. We also would like to acknowledge the University of the West of England Bristol UK for hosting the first author to carry out some initial simulation work.

References

1. Dolling D.S., Fifty years of shock-wave/boundary-layer interaction research: What next? *AIAA Journal*, 2001. 39(8): 1517-1531.
2. Settles G.S., and Dodson L.J., Hypersonic shock/boundary-layer interaction database. *NASA STI/Recon Technical Report N*, 1991. 93: 24526.
3. Delery J.M., and Panaras A.G., Shock Wave Boundary-Layer Interaction in High Mach Number Flows. *AGARD Advisory Report AR-319* 1996. No. 1 pp. 2.1-2.61.
4. Green J.E., Interactions between shock waves and turbulent boundary layers. *Progress in Aerospace Sciences*, 1970. 11: 235-340.
5. Adamson Jr. T.C., and Messiter A.F., Analysis of two-dimensional interactions between shock waves and boundary layers. *Annual Review of Fluid Mechanics*, 1980. 12(1): 103-138.
6. Delery J.M., Shock phenomena in high speed aerodynamics: still a source of major concern. *Aeronautical Journal*, 1999. 103(1019): 19-34.
7. Knight D., Yan H., Panaras A.G., and Zheltovodov A.A., Advances in CFD prediction of shock wave turbulent boundary layer interactions. *Progress in Aerospace Sciences*, 2003. 39(2): 121-184.
8. Babinsky H.M., and Harvey, J.K., *Shock wave-boundary-layer interactions*. 2011, Cambridge University Press.
9. Georgiadis N.J., Rizzetta D.P., and Fureby C., Large-eddy simulation: current capabilities, recommended practices, and future research. *AIAA Journal*, 2010. 48(8): 1772-1784.
10. Moin P., and Krishnan M., Direct numerical simulation: a tool in turbulence research. *Annual Review of Fluid Mechanics*, 1998. 30(1): 539-578.
11. Viswanath P.R., Shock-wave-turbulent-boundary-layer interaction and its control: A survey of recent developments. *Sadhana*, 1988. 12(1-2): 45-104.
12. Lin J.C., Review of research on low-profile vortex generators to control boundary-layer separation. *Progress in Aerospace Sciences*, 2002. 38(4): 389-420.
13. Lu F.K., Li Q., and Liu C., Microvortex generators in high-speed flow. *Progress in Aerospace Sciences*, 2012. 53: 30-45.
14. Blinde P.L., Humble R.A., van Oudheusden B.W. and Scarano F., Effects of micro-ramps on a shock wave/turbulent boundary layer interaction. *Shock Waves*, 2009. 19(6): 507-520.
15. Gefroh D., Loth E., Dutton C., and Hafenrichter E., Aeroelastically deflecting flaps for shock/boundary-layer interaction control. *Journal of Fluids and Structures*, 2003. 17(7): 1001-1016.
16. Srinivasan K.R., Loth E., and Dutton C., Aerodynamics of recirculating flow control devices for normal shock/boundary-layer interactions. *AIAA Journal*, 2006. 44(4): 751-763.
17. Popkin S.H., Taylor, T.M., and Cybyk B.Z., Development and Application of the SparkJet Actuator for high-speed flow control. *Johns Hopkins APL technical digest*, 2013. 32(1): 404-418.
18. Doerffer P.P., and Bohning R., Shock wave–boundary layer interaction control by wall ventilation. *Aerospace Science and Technology*, 2003. 7(3): 171-179.
19. Pasquariello V., Grilli M., Hickel S., and Adams N.A., Large-eddy simulation of passive shock-wave/boundary-layer interaction control. *International Journal of Heat and Fluid Flow*, 2014. 49: 116-127.
20. Land H.B. III, Grossman K.R., Cybyk B.Z., and VanWie D.M., Solid State Supersonic Flow Actuator and Method of Use. 2003, *U.S. Patent 7,988,103*
21. Reedy T.M., Kale N.V., Dutton J.C., and Elliott G.S., Experimental characterization of a pulsed plasma jet. *AIAA Journal*, 2013. 51(8): 2027-2031.

22. Belinger A., Naudé N., Cambronne J.P., and Caruana D., Plasma synthetic jet actuator: electrical and optical analysis of the discharge. *Journal of Physics D: Applied Physics*, 2014. 47(34): 345202.
23. Caruana D., Barricau P., and Gleyzes C., Separation control with plasma synthetic jet actuators. *International Journal of Aerodynamics*, 2013. 3(1): 71-83.
24. Cybyk B.Z., Grossman K.R., Jordan W., Chen J., and Katz J., Single-pulse performance of the sparkjet flow control actuator. *AIAA paper*, 2005. 401: 2005.
25. Cybyk B.Z., Simon D.H., Land H., Chen J., and Katz J., Experimental characterization of a supersonic flow control actuator. *AIAA paper*, 2006. 478: 2006.
26. Cybyk B.Z., Wilkerson, J.T., and Grossman, K.R., *Performance characteristics of the sparkjet flow control actuator*. In *2nd AIAA Flow Control Conference*. 2004.
27. Jin D., Li Y.H., Jia M., Song H.M., Cui W. Sun Q. and Li F.Y., Experimental characterization of the plasma synthetic jet actuator. *Plasma Science and Technology*, 2013. 15(10): 1034.
28. Grossman K.R, Cybyk B.Z., and VanWie D.M., Sparkjet actuators for flow control. *AIAA paper*, 2003. 57: 2003.
29. Haack S.J., Taylor, T.M., Cybyk B.Z., Foster, C., and Alvi, F., *Experimental Estimation of SparkJet Efficiency*. In *42nd AIAA Plasmadynamics and Lasers Conference*. 2011.
30. Haack S.J., Land H.B., Cybyk B., Ko H.S., and Katz J., *Characterization of a high-speed flow control actuator using digital speckle tomography and PIV*. In *4th AIAA Flow Control Conference*. 2008.
31. Ko H.S., Haack, S.J., Land H.B., Cybyk B., Katz J., and Kim H.J., Analysis of flow distribution from high-speed flow actuator using particle image velocimetry and digital speckle tomography. *Flow Measurement and Instrumentation*, 2010. 21(4): 443-453.
32. Inagaki M., Kondoh T., and Nagano Y., A mixed-time-scale SGS model with fixed model-parameters for practical LES. *Journal of Fluids Engineering*, 2005. 127(1): 1-13.
33. Vreman B., Direct and large-eddy simulation of the compressible turbulent mixing layer. *PhD Thesis, Department of Applied Mathematics, University of Twente.*, 1995.
34. Carpenter M.H., Nordström J., and Gottlieb D., A stable and conservative interface treatment of arbitrary spatial accuracy. *Journal of Computational Physics*, 1999. 148(2): 341-365.
35. Gottlieb S., and Shu C.W., Total variation diminishing Runge-Kutta schemes. *Mathematics of Computation of the American Mathematical Society*, 1998. 67(221): 73-85.
36. Yee H.C. and Sjögreen B., Designing adaptive low-dissipative high order schemes for long-time integrations, *Turbulent Flow Computation*. 2002, Springer. 141-198.
37. Yee H.C, Sandham N.D., and Djomehri M.J., Low-dissipative high-order shock-capturing methods using characteristic-based filters. *Journal of Computational Physics*, 1999. 150(1): 199-238.
38. Ducros F., Ferrand V., Nicoud F., Weber C., Darracq D., Gacherieu C., and Poinsot T., Large-eddy simulation of the shock/turbulence interaction. *Journal of Computational Physics*, 1999. 152(2): 517-549.
39. Yao Y., Shang Z., Castagna J., Sandham N. D., Johnstone R., Sandberg R.D., Suponitsky V., Redford J.A., Jones L.E., and De Tullio, N., Re-engineering a DNS code for high-performance computation of turbulent flows. *Proceedings of the 47th Aerospace Sciences Meeting Including the New Horizons Forum and Aerospace Exposition* 2009, *AIAA paper*, 2009-566.
40. Poinsot T.J., and Lelef S.K., Boundary conditions for direct simulations of compressible viscous flows. *Journal of computational physics*, 1992. 101(1): 104-129.
41. Touber E., and Sandham, N.D., Large-eddy simulations of an oblique shock impinging on a turbulent boundary layer: low-frequency mechanisms. *18th International Shock Interaction Symposium*, 2008.
42. Dupont P., Haddad C., and Debieve J. F., Space and time organization in a shock-induced separated boundary layer. *Journal of Fluid Mechanics*, 2006. 559: 255.

43. Garnier E., Sagaut P., and Deville M., Large eddy simulation of shock/boundary-layer interaction. *AIAA Journal*, 2002. 40(10): 1935-1944.
44. Touber E., and Sandham N.D., Large-eddy simulation of low-frequency unsteadiness in a turbulent shock-induced separation bubble. *Theoretical and Computational Fluid Dynamics*, 2009. 23(2): 79-107.
45. Garnier E., Nikolaus A., and Sagaut P., *Large eddy simulation for compressible flows*. 2009: Springer Science & Business Media.
46. Touber E., and Sandham N.D., Low-order stochastic modelling of low-frequency motions in reflected shock-wave/boundary-layer interactions. *Journal of Fluid Mechanics*, 2011. 671: 417-465.
47. Adelgren R.G., Elliott G.S., Knight D., Zheltovodov A.A., and Beutner T.J., Energy deposition in supersonic flows. *AIAA paper*, 2001-885, 2001.
48. Zheltovodov A.A., Pimonov E.A., and Knight D.D., Numerical modeling of vortex/shock wave interaction and its transformation by localized energy deposition. *Shock Waves*, 2007. 17(4): 273-290.